1

Tendon Stress Evaluation of Unbonded Post-Tensioned Concrete Segmental Bridges with Two-variable Response Surfaces

Rudhra Halder[a,c], Terry Y.P. Yuen[a,b*], Wang-Wen Chen[d], Xiangming Zhou[e], Trissa Deb[a,b], Hexin Zhang[f], Tzu-Han Wen[a,b]

[a] Department of Civil Engineering, National Yang Ming Chiao Tung University, Hsinchu 30010, Taiwan (R.O.C.)
[b] Department of Civil Engineering, National Chiao Tung University, Hsinchu, 30010, Taiwan (R.O.C.)
[c] Department of Civil Engineering, Manipal University Jaipur, Rajasthan, India
[d] CECI Engineering Consultants, Inc., Taipei, Taiwan (R.O.C.)
[e] Department of Civil & Environmental Engineering, Brunel University London, Uxbridge, Middlesex UB8 3PH, United Kingdom
[f] School of Engineering and the Built Environment, Edinburgh Napier University, Edinburgh, Scotland, United Kingdom

ABSTRACT

This paper comprehensively studied the combined effects of prestress change and aspect ratios on the nonlinear structural performances of externally prestressed precast concrete segmental bridges (PCSB). An experimentally validated discrete-finite element model was adopted and various analytical cases were generated with variable span lengths. Furthermore, a simulation study is performed considering the change in prestress level to understand its effect on structural response, failure behaviour, and tendon stress at the ultimate limit state (ULS). The result showed that the stress in the unbonded tendon before the failure stage varies from 0.79 to $1.03 f_{py}$ for the shorter tendon (T6L) and 0.66 to $0.94 f_{py}$ for the longer tendon (T5L), and on comparing with the prediction of the existing codes, the stresses are highly underestimated. However, for the typical prestress level of around $0.6 - 0.7 f_{pu}$, the ACI318 code could quite well predict the ultimate tendon stress change. To establish the dependency of stress in the unbonded tendon at ULS to the normalized prestress factor (α) associated with the aspect ratio (L/d), the response surface methodology (RSM) was implemented. The mediocre prediction of one-variable linear regression analysis concludes the dependency of the combined effects of the two variables on the response variables. The 3rd order two-variable response surfaces were able to predict an increase in stress and total stress of tendon at the ULS with high goodness-of-fit values of 0.97 and 0.92 respectively.

Keywords: Precast concrete segmental bridge; externally unbonded tendon; discrete finite element model; response surface methodology; prestress change

---

* Corresponding author. E-mail address: terryyyp@nctu.edu.tw

1. Introduction

The precast concrete segmental bridges (PCSBs) gain rapid acceptance worldwide and become a favorable choice to achieve a longer span for bridges. Being cost-effective, durable, rapid construction, they also provide excellent serviceability, aesthetically pleasing, and minimum impact on the environment [1,2]. In contrast to the monolithic bridge, the precast concrete bridge consists of precast segments and the joints may be dry or epoxy coated. The precast segments are held together by prestress tendons, either bonded or unbonded and shear key at joint. The keys are essential for alignment and shear transfer [3–6]. Due to the ease of inspection for corrosion and replacement, constructions with externally unbonded tendons have become more popular in recent years. However, the flexural behaviour of unbonded PCSBs is complicated because the prestress force is indirectly transferred from the tendons to the concrete girder through deviators and end-anchorages. Since the plane section remains plane assumption would be no longer valid for the structures with unbonded tensions, they cannot be modeled and analyzed by the conventional beam theory. Thus, the prediction of unbonded tendon stress and load-carrying capacity of PCSB at the failure using existing code can be challenging [7–9]. Over the decades, the unbonded precast segmental bridges become highly popular, even the structure evinces complicate and uncertain behaviour, mainly because of deadweight reduction which proven to be cost-effective but also provides safe and easy replacement of tendon [10] and ease in the inspection of the tendon while in utilization [11]. The cause of the reduction in strength and stiffness of the segmental bridge can also be due to improper workmanship, which causes concrete spalling and flaking [12] and corrosion of unprotected tendons in the wet environment [13]. Such factors can add up to the loss of prestressing force and combine with the long-term losses (creep, shrinkage, steel relaxation) can affect the load-carrying capacity and also trigger premature decompression of the structure [14]. The premature decompression can cause significant reduction in flexural stiffness of the structure and increases the risk of vulnerability.

Several studies on the behaviour of segmental concrete structures can be found in the literature. Aparicio et al. [15] presented a comparative study between the monolithic beam and externally prestressed concrete box girders. The beams are categorically tested under flexural and combined flexural and shear load. The study concluded that the ultimate load-carrying capacity of prestressed beams was influenced by the joint opening and tendon length. Turmo et al. [16–18] developed a numerical method and investigated the effect of change in prestress level on the shear behaviour of concrete segmental beams, which had dry joints and external tendons, under combined shear and flexure. The result showed that fracture in concrete initiate from the joint interface and spread towards the point of loading. The increase in the prestress level has an impact on the joint opening load and increases the load-carrying capacity of PCSBs. To investigate the effect of shear span ratios (a/h)

on prestress segmental beams, Li et al. [19,20] experimented on prestress beams with unbonded tendons subjected to both shear and flexural load. The shear resistance of the joint of the tested beams decreased with increasing a/h and the failure mode was affected by the shear-span.

Recently, the application of hybrid internal and external tendon in PCSB has become increasingly popular. The ductility can be improved owing to internal tendons and external tendons are accessible for maintenance, which attests for better performance over the "classical" prestress bridges. Studies on the precast segmental beams with hybrid tendons under combined bending, shear, and torsional loading [7,21–23] is the current research trend about post-tensioned concrete segmental bridges. It can be seen from previous studies which conducted only experimental investigation considering the effect of change in effective prestress on the behaviour of PCSBs, but very few have presented rigorous numerical models of the segmented bridge with externally prestress tendon. The structural behaviour of post-tensioned members with unbonded tendons is complicated in particular during the inelastic deformation stage as the members do not follow the elementary beam behaviour [24,25]. In a recent study, experimentally validated three-dimensional numerical models of PCSBs that employed the advanced discrete-finite element modelling (DFEM) approach was proposed and validated against test results [9]. The validated model effectively captures both the global and local responses such as local tendon stress change, duct slip, and damage patterns of PCSBs. In this study, the concurrent effects of the change in prestress level and aspect ratio on the structural performances of PCSBs regarding load-carrying and deflection capacity, stress change in the tendon at the ultimate limit state (ULS) will be comprehensively addressed based on the validated DFEM approach.

This study investigates the combined effects of two essential parameters: the aspect ratio (L/d) and the change in prestress level as quantified by a proposed normalized prestress factor (α) on the global and local responses of the PCSB. The influence of aspect ratio and effective prestress on deformation and moment characteristics, tendon strain and slip variations, and tendon stress variations at ULS are evaluated through numerical analysis. Finally, a comprehensive and quantified assessment of the parameter influence on the stress increase and total stress in unbonded tendons is undertaken with the response surface methodology (RSM) and the objective is to provide an accurate expression for rational evaluation of the stress in unbonded tendons in such box girder segmental type structures.

2. DFEM of Precast Concrete Segmental Bridges

2.1 *Prototype bridge structure*

In this study, a highway bridge span consisting of 14 segments is an integrated part of the Bangkok expressway project considered as a prototype. The overall length of the span was 44.25 m, and the precast reinforced concrete box-girder segment has the height and width of 2.4 m and 10.2 m respectively. The schematic diagram and tendon layout in the bridge segments are shown in Fig. 1. AASHTO specifications [26,27] are followed in the design of the highway bridge. The bridge was externally prestressed with twelve unbonded tendons in which ten tendons are longer with draped profile and two tendons are short and straight formed from 19K15 strands and 12K15 strands, respectively. The longer (T1-T5) tendons are connected to the bridge span at the 4th, 7th and 11th segments by deviators and anchored at the ends, while the shorter (T6) tendons are connected through deviators at the 7th segments and anchored at 4th and 1st segments. The segments were interlocked by dry shear keys. Descriptive details of the full-scale destructive experiment of the highway bridge prototype are materialized in Takebayashi *et al.* [28]. Table 1 shows the properties of concrete, prestressing, and non-prestressing materials of the prototype.
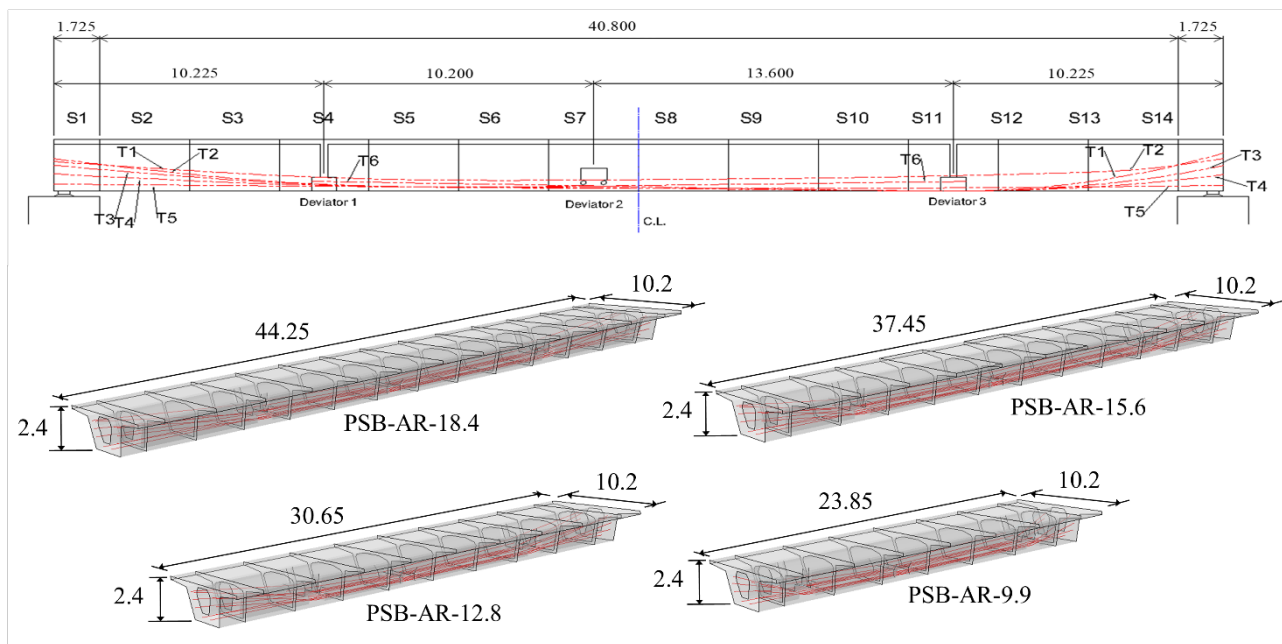
Fig 1. Schematic diagram with tendon profile of prototype PCSB (the non-prestressing reinforcement is not shown) [28] and geometric details of numerical models (dimensions in m).

Table 1. Details of material properties for the prototype [28].

Material	Young's modulus (GPa)	Strength (MPa)
Concrete	43	$f_{cc} = 55\text{-}62$
Rebar	210	$f_{sy} = 390$
Prestressing Tendons	193	$f_{pu} = 1920$

2.2   *DFE modelling and contact mechanism*

The effective prestress f_{pe} developed in the external tendons after post-tensioning found to be $0.62f_{pe}$ $i.e, 1198MPa$, which is equal to the prestress force P_e of 38,433 kN as mentioned in the test by Takebayashi *et al.* [28]. The application of vertical load was carried out by consistently increasing the weight of the steel billets placed between 4th-6th and 9th-11th segments till the collapse of the bridge. The bridge behaviour at several important loading stages including the decompression and the ultimate load was observed during the experiment and the recorded weight (in tons) of steel billets were 374.8, 562.1, 902.2, and 909.14, respectively. The corresponding applied mid-span moment for each stage was 24.6 MN·m, 36.5 MN·m, 57.7 MN·m, and 58.2 MN·m. The extensive test result data can further utilize to develop detailed and reliable numerical models [29], to successfully capture the global as well as local responses in terms of load-displacement and stress-strain relationship as observed in the experiment.

To simulate the destructive test by Takebayashi *et al.* [28], rigorous and validated discrete finite element (DFEM) models were developed using Abaqus/Explicit [30,31]. A mesh convergence study of the numerical analysis was performed by varying the element sizes from 1000 mm, 800 mm, 600 mm, to 400 mm. It was cocluded that the element size of 600 mm gave the optimal balance between the computational time and accuracy against the test results. The use of extremely small stable time increment ($< 1e^{-5}$s in this study), which depdens on the element size, material stiffness, and damaping, is required in the explicit algorithm to achieve stability condition which also leads to high computational demand. But the explicit algorithm is advantageous in this study that involes highly nonlinear analysis of contact, coupled damage-plastic, and connector modelling. This is because explicit algorithm allows the solution to proceed without requiring tangent stiffness matrices to be formed. In addition to the original model of the prototype bridge denoted as PSB-AR-18.4, three models were developed with different span lengths of 37.45 m, 30.65 m, and 23.85 m, will be referred to as PSB-AR-15.6, PSB-AR-12.8, and PSB-AR-9.9 respectively, for the comprehensive parametric study on the combined effects of prestress change and aspect ratio. The design parameters of the four models are summarized in Table 2. Where, β_i is the coefficient defined as the change in prestress level and α_i is the proposed normalized prestress factor defined as the ratio of prestress moment to the self-weight moment. The concrete bridge and shear keys are modelled with the built-in 3D linear brick, hexahedral elements (C3D8). The body of the shear key is embedded in the adjoining segment and the base of the shear key is tied to the concrete surface. Linear 3D beam elements (B31) are used to mesh the post-tensioning tendons, while the non-prestressing steel reinforcements were meshed by the two-node 3D truss elements (T3D2). The embedded region constraints are used to model the confinement of the rebar by the concrete. The anchorages of tendons at the end concrete segments

152 are modelled using a kinematic coupling. At the contact interface between the bridge segments, the
153 contact interactions are implemented. As per the EC2 [32] recommendation, the friction coefficient
154 is taken as $\mu = 0.6$, and normal contact stiffness $S_n = 520\,kN/mm$ is specified. The contact
155 interaction allow surfaces to transfer the compressive force and friction through the interface without
156 penetration. The tangential behaviour is modelled by Columb friction model such that there would
157 be no slip of the contacting surfaces before the shear friction given by $\mu\sigma_N$ is excceded. Once the
158 shear firiction is excceded, the contacting surfaces slide in a perfect plastic manner. The modelling
159 methodology which integrates the deformable elements and the contact interaction between element
160 surfaces is called discrete finite element modelling (DEFM) and such approach is particularly suitable
161 for modelling crack opening and interacting problems (e.g. [30,33,34]) which are similar to the joint
162 opening behaviour in the bridge segments. The contact of the prestressing tendons at the deviators
163 modelled with a translator to allow movement of tendons only along the longitudinal direction of the
164 bridge. Material properties and constitutive model

165 *2.2.1 Concrete*

166 This study adopted the Barcelona model [35], which proposed a non-associated elastoplastic
167 constitutive model for concrete. The yield criterion is given by

$$F = \frac{1}{1-\alpha}\left[\sqrt{3J_2} + \alpha I_1 + \beta(\tilde{\varepsilon}_p)\langle\sigma_{max}\rangle - \gamma\langle-\sigma_{max}\rangle\right] - c(\tilde{\varepsilon}_p) \tag{1}$$

$$\langle\sigma_{max}\rangle = \begin{cases} \sigma_{max}, & if\,\sigma_{max} \geq 0 \\ 0, & if\,\sigma_{max} \leq 0 \end{cases} \tag{2}$$

170 where $\tilde{\varepsilon}_p$ is the equivalent plastic strain; β, and c are introduced as hardening and softening
171 parameters. β can be obtained from the ratio of uniaxial compressive strength to uniaxial tensile
172 strength and c is concrete compressive cohesion strength. The material parameters α and γ are
173 dimensionless constants that govern the shape of the yield surface in the deviatoric and meridian
174 planes, respectively. The yield function from Eq. (1) can reduce to the Drucker-Prager yield criterion
175 if the maximum principal (tensile) stress σ_{max} is considered zero (Eq. (2)). In the present model,
176 Drucker-Prager yield function in terms of the eccentricity of the hyperbolic function (e) and angle of
177 dilation (ψ) have been chosen for flow potential defined by Eq. (3).

$$G = \sqrt{J_2 + \left(ef_t(\tilde{\varepsilon}_p)\tan\psi\right)^2} + I_1\tan\psi \tag{3}$$

179 The inelastic deformation in brittle and quasi-brittle materials is either controlled by tensile fracture
180 or shear friction under confining compression. While the inelastic strain increment is governed by
181 the dilation angle ψ under high compression, the tensile fracture strain shall be normal to the
182 maximum tensile stress direction, i.e. the flow is associated under pure tension. Therefore, the second

term in Eq. (3) is used to model the behaviour of the inelastic strain flow direction in the region dominated by tension.

Table 2. Design parameters of the PCSB models.

Model name	L (m)	L/d	W (kN)	M_{SW} (kN·m)	P_e (kN)	β_i	M_{PE}^i (kN·m)	α_i
						0.1	9223.92	0.4
						0.22	18447.84	1.0
						0.4	36895.68	1.7
PSB-AR-18.4	44.25	18.4	5645.40	20817.41	38433	0.6	55343.52	2.6
						0.8	73791.36	3.5
						1.0	92239.20	4.4
						1.2	110687.04	5.3
						0.1	9223.92	0.6
						0.16	14758.27	1.0
						0.28	25826.97	1.7
PSB-AR-15.6	37.45	15.6	4853.20	15146.02	38433	0.4	36895.68	2.4
						0.6	55343.52	3.6
						0.72	66412.22	4.4
						0.8	73791.36	4.8
						0.07	6456.744	0.6
						0.1	9223.92	1.0
						0.2	18447.84	1.7
PSB-AR-12.8	30.65	12.8	4061.04	10372.57	38433	0.31	28594.15	2.8
						0.43	39662.85	3.8
						0.49	45197.21	4.4
						0.54	49809.16	4.8
						0.04	3689.56	0.6
						0.07	6456.74	1.0
						0.12	11068.70	1.7
PSB-AR-9.9	23.85	9.9	3268.90	6496.94	38433	0.20	18447.84	2.8
						0.27	24904.58	3.8
						0.31	28594.15	4.4
						0.34	31361.32	4.8

The relationship of the first invariants I_1 and the second invariants J_2 with the stress tensor σ_{ij} is defined as:

$$I_1 = \sigma_{ii}; J_2 = \frac{1}{2}\left(\sigma_{ij} - \sigma_{kk}\delta_{ij}/3\right)^2 \tag{4}$$

Kratzig and Polling (2004) model [36] is adopted to model the nonlinear uniaxial compressive stress-strain curve $\sigma_c(\varepsilon)$ for $\varepsilon \geq 0$ given by:

$$\sigma_c(\varepsilon) = \begin{cases} \dfrac{E_{ci}\frac{\varepsilon}{f_{cc}} + \left(\frac{\varepsilon}{\varepsilon_{cc}}\right)^2}{1 - \frac{\varepsilon}{\varepsilon_{cc}}\left(E_{ci}\frac{\varepsilon}{f_{cc}} - 2\right)} f_{cc} & (\varepsilon > \varepsilon_{cc}) \\[4mm] \left(\dfrac{2 + \gamma_c f_{cc}\varepsilon_{cc}}{2f_{cc}} + \gamma_c\varepsilon + \dfrac{\gamma_c}{2\varepsilon_{cc}}\varepsilon^2\right)^{-1} & (\varepsilon \leq \varepsilon_{cc}) \end{cases} \tag{5}$$

where E_{ci} and ε_{cc} are the initial young's modulus and the corresponding strain at the maximum uniaxial compressive strength (f_{cc}), respectively. The material parameter governing the area of the tensile stress-strain diagram is defined by γ_c in Eq. (6). To reduce the mesh sensitivity of the post-peak strain-softening behaviour, the stress-strain model proposed by Kratzig and Polling is used as it

$$\gamma_c = \frac{\pi^2 f_{cc}\varepsilon_{cc}}{2\left[\dfrac{G_c}{l_{eq}} - \dfrac{1}{2}f_{cc}\left(\varepsilon_{cc}(1 - b_c) + b_c\dfrac{f_{cc}}{E_c}\right)\right]^2} \tag{6}$$

depends on the tensile fracture and compressive crushing energies.

where l_{eq} and b_c are the characteristic length of elements, and a dimensionless constant to differ damaging parts from plastic in inelastic strains, respectively. Furthermore, the CEB-FIP (2010) model [37] is adopted to model the inelastic uniaxial tensile stress-strain behaviour $\sigma_t(\varepsilon)$ for $\varepsilon < 0$ as follows. G_c is the energy release during the compressive crushing process and can be calculated by Eq. (7) [38]

$$G_c = 8.8\sqrt{f_c'} \qquad \text{(N, mm)} \tag{7}$$

$$\sigma_t(\varepsilon) = \begin{cases} E_{ci}\varepsilon & (\sigma_t \leq 0.9 f_{ctm}) \\[2mm] f_{ctm}\left(1 - 0.1\dfrac{0.00015 - \varepsilon}{0.00015 - 0.9 f_{ctm}/E_{ci}}\right) & (0.9 f_{ctm} < \sigma_t \leq f_{ctm}) \\[2mm] f_{ctm}\left(1 - 0.8\dfrac{\varepsilon}{\varepsilon_1}\right) & (\varepsilon_{ct} < \varepsilon \leq \varepsilon_1) \\[2mm] f_{ctm}\left(0.25 - 0.05\dfrac{\varepsilon}{\varepsilon_1}\right) & (\varepsilon_1 < \varepsilon \leq \varepsilon_2) \end{cases} \tag{8}$$

where f_{ctm} is the peak tensile strength, $\varepsilon_1 = G_t/f_{ctm}l_{eq}$, and $\varepsilon_c = 5G_t/f_{ctm}l_{eq}$ in which G_t is the mode I fracture energy which can be calculated by Eq. (9) according to CEB-FIP model code (2010)

$$G_t = 73 f_c'^{0.18} \qquad \text{(N, mm)} \tag{9}$$

The details of material parameters are presented in Table 3.

Table 3. Parameters of the material modelling.

Material	Parameter	Value
Concrete	Compressive strength, f_{cc}	60 MPa
	Strain at corresponding f_{cc}, ε_{cc}	0.0022
	Young's modulus, E_c	43 GPa
	Poisson's ratio	0.2
	Parameter (yield surface), α	0.12
	Parameter (yield surface), γ	3
	Eccentricity (flow surface), e	0.1
	The angle of dilation, ψ	20°
	Compressive crushing energy, G_c	56.2 N/mm
	Tensile fracture energy, G_t	0.1423 N/mm
	Damage parameter in compression, b_c	0.5
	The characteristic length of elements, l_{eq}	600 mm
Rebar	Yield strength, f_{sy} (MPa)	390
	Young's modulus, E_s (GPa)	210
	Poisson's ratio	0.3
Tendons	Yield strength, f_{py}	1728 MPa
	Breaking strength, f_{pu}	1920 MPa
	Young's modulus, E_s	193 GPa
	Strain at the peak strength, ε_{pu}	0.03
	Poisson's ratio	0.28
	Total prestressing force	38433 kN

The above constitutive models for the stress-strain relationship of concrete are a form of the smeared-crack model. The crack initiate when the tensile strength is exceeded by the maximum principal stress. The crack propagation is governed by the shape of the tensile-softening curve and fracture energy. To assure the mesh objectivity, the fracture energy (G_t) dependent post-peak stress-strain relationship is associated with characteristics length of the finite element(l_{eq}).

2.2.2 Rebar and prestressing tendons

A linear perfect-plastic model is used for normal steel rebar and the tendon's stress-strain behaviour is assumed to be bilinear. The tensioning of the tendons in the models can be carried out using the thermal load-induced deformation method [39] with a negative temperature change as a predefined field in Abaqus [40]. The required temperature change to achieve the target prestressing force can be calculated by the following equation [39]:

$$\Delta T = -\frac{P_e}{c \cdot E_{ps} \cdot A_{ps}} \tag{10}$$

where $c = 13\,^{o}C^{-1}$ is the thermal expansion coefficient for the prestressing tendons.

2.3 *Comparisons of the DFEM simulated and test results*

The developed DFEM of the segmental bridge had been successfully applied to simulate different loading tests on PCSBs [28,41] and the detailed validation results can be found in [30]. This section briefly demonstrates the comparison between the simulated and tested results. Besides the above-mentioned full-scale loading test by Takebayashi *et al.*[28], the tests on the effects of different shear-spans by Jiang *et al.* [41] were also simulated to test the capability of the proposed DFEM in capturing the behaviour of PT-PCSBs with different aspect ratios.

As observed in Fig. 2(a), the simulations can well capture the tested load-deflection responses obtained by Jiang *et al.* [41]. The curve shows the linear and nonlinear relationship before cracking to until failure. The simulated damage patterns of the specimens with low shear span (D.15-40-N) and long shear span (D2.5-50-N) also match the test results as shown in Fig. 2(b). Furthermore, the comparison of the simulated deflection profile with the experimental results for various defined loading stages in Takebayashi *et al.* [28] is shown in Fig. 2(c), the simulations can accurately reproduce the detailed asymmetric deflection profile because of the unsymmetrical layout of the tendon. The maximum deflection ($\delta_{8-9}^{BF} = -338\ mm$ & $M_{max}^{BF} = 58.2$ kNm) observed at the joint located between 8th segment and 9th segment and experience wide opening of joint just before the failure state (BF). In addition, a significant state defined as Decompression state (DC) ($\delta_{8-9}^{DC} = -49$ mm & $M_{max}^{DC} = 36.5$ kNm) can be witnesses during simulation where the compressive stress induced by prestressing happened to neutralize due to the application of vertical load.. The DC state remarked the significant reduction in stiffness of PCSBs and such behaviour is also well captured by the proposed DFEM.

In addition to the global load-deflection behaviour, the local behaviour such as the change in strain and duct slips (relative to the deviators) of tendons are also well reflected by the DFEM. The simulated duct slips of longer tendons T5 (Fig. 2(d)) are remarkably close to the experimental results [28]. The simulations produce only slightly smaller duct slips in comparison with experimental results which may be due to the assumption of linear slip-restoring force relationship. From the above discussion, it is evident that the proposed numerical modelling method is capable to simulate global behaviour as well as local responses. A comprehensive study on the numerical modelling and validation of the model can be found in Yuen *et al.* [30]. Extensive parametric studies were then

258 carried out with the validated model to study the flexural performance of externally prestressed PCSB

259 and the results are presented in the next section.

260

(a)

(b)

(c)

(d)
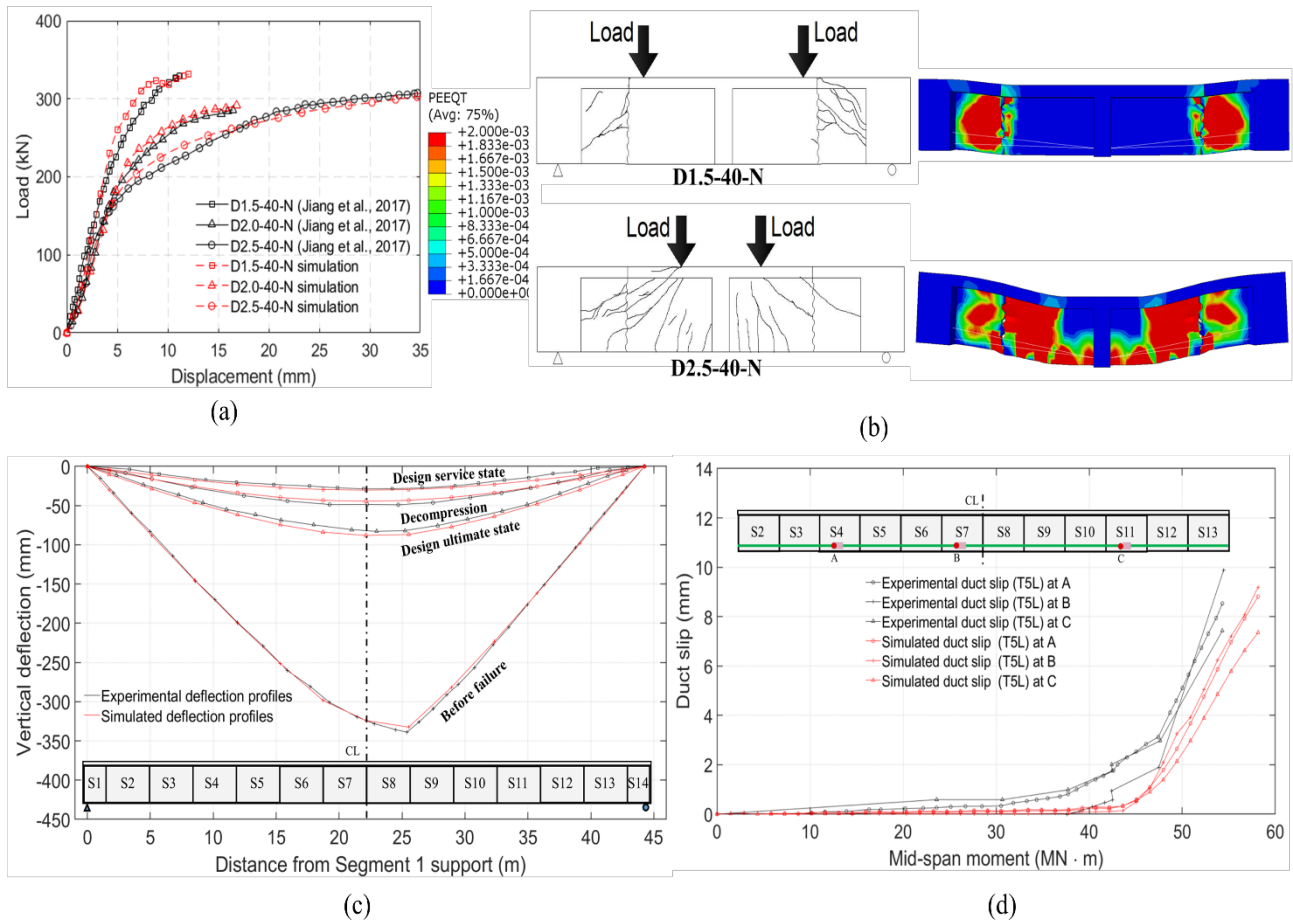
261

262 **Fig 2.** (a) Comparison of the simulated and experimental (a) load-deflection curves and (b) crack

263 patterns by Jiang *et al.* [41]; (b) comparison of the simulated and experimental (c) deflection profile

264 and (d) duct slips of T5L at different loading stages by Takebayashi *et al.* [28].

3. Combined Effects of Prestress Change and Aspect Ratio

266 In this section, the combined effect of prestress change and aspect ratio on the nonlinear structural

267 behaviour performance of PT-PCSBs with the unbonded tendon are thoroughly investigated. As

268 shown in Fig.1 and Table 1, the four models have the same concrete segment configurations,

269 properties of materials and tendons, the tendon profiles except for the span length. The span lengths

270 of the four models are 44.25 m, 37.45 m, 30.65 m, and 23.85 m corresponding to the aspect ratios of

271 18.4, 15.6, 12.8, and 9.9 respectively. To obtain generalized analysis results, a dimensionless

272 parameter α_i defined as the ratio of the maximum prestress moment M_{PE}^i to the maximum moment

273 M_{SW} induced by the self-weight of the bridge is introduced as

$$\alpha_i = \frac{M_{PE}^i}{M_{SW}} \tag{11}$$

where $M_{PE}^i = \beta_i P_e d$, in which P_e is the effective prestress force and β is the fraction value which increases from 0.10 to 0.8 for PSB-AR-15.6, 0.07 to 0.54 for PSB-AR-12.8, and 0.04 to 0.34 for PSB-AR-9.9. The value increases to 1.2 for PSB-AR-18.4 and $d = 2.4\,m$ is the depth of the segment. $M_{SW} = (WL/12)$, in which W is the weight of the whole girder and L is the span length. The values of normalized prestress factor, prestress moment and self-weight moment are shown in Table 2.
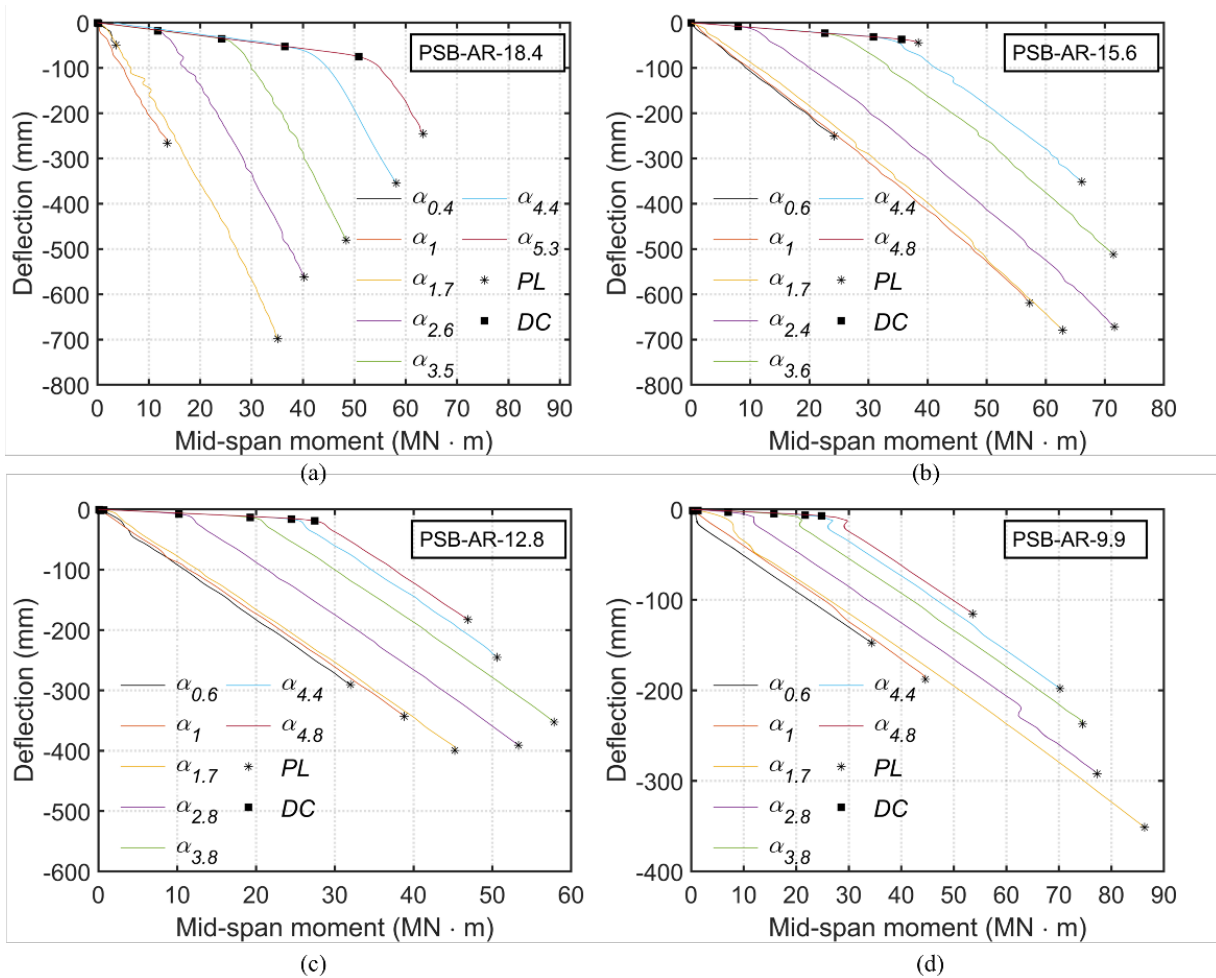
3.1   *Mid-span moment versus deflection*

The mid-span moment versus deflection curves for all four models at the different prestressing levels is shown in Figs. 3(a-d). The mid-span moment versus deflection curves was divided into two stages – decompression (DC) and Peak Load (PL). The upward deflection of the structure due to prestressing is called camber and the state when the deflection caused by vertical loading overcome the camber regard as the onset of decompression of structure. The moment at DC state is defined as the "cracking" moment which also triggers the opening of joints and increases with the increase in effective prestress. Before the DC stage, all the models exhibit a linear relationship between the applied moment and deflection with high stiffness. At the PL stage, the joints in the segmental bridges began to open, and thereafter the stiffness massively reduces with a non-linear softening load-deflection behaviour up to failure. The change from DC to PL stage is due to the opening of the joint between S8-S9 (located at left to the middle of span) for PSB-AR-18.4, PSB-AR-15.6, and joint at the middle of span for the other two models.

As observed in Fig. 3, an increase in prestress force results in a decrease in ultimate deflection of PCSBs significantly but increases the moment resistance at both DC and PL stages. The displacement and mid-span moments corresponding to the two stages (DC and PL) are shown in Table 4. As the normalized prestress factor (α) increases from 1.7 to 4.4, the maximum moment at PL increases by 65.67%, 5.17%, 11.65% for PSB-AR-18.4, PSB-AR-15.6, PSB-AR-12.8 except PSB-AR-9.9 model, which shows a decrease of 18.63%. Similarly, all the models exhibit a decrease in deflection at the ultimate stage by 49.6%, 48.3%, 38.6%, and 43.6% at higher prestress force.

This behaviour significantly affects the design of PCSBs regarding the serviceability deflection limits. When the normalized prestress factor is above 4.4 in Fig. 3(b), the bridge model PSB-AR-15.6 attains failure immediately after the opening of joints. In the case of $\alpha = 4.8$, the corresponding moment at DC is 35.62 MN.m and the ultimate moment is 38.44 MNm due to the concrete crushing.

Fig. 3. Mid-span moment versus deflection.

3.2 *Deflection profiles*

The deflection profile at peak load (PL) stage along the length of the segmental bridge subjected to increasing prestressing force is shown in Figs. 4(a-d). Similarly, Figs. 5(a-d) shows the deflection profile at the decompression (DC) stage along the length of the model subjected to varying levels of prestressing force. The deflection is measured concerning the bridge profile after the transferring of prestress and the addition of self-weight. As shown in Fig. 4, the locations of the maximum deflection in PSB-AR-18.4 and PSB-AR-15.6 models are at S8-S9 (left to the center of span) in contrast to the behaviour of monolithic beam, where maximum deflection occurs at mid-span, similar behaviour observed in model PSB-AR-12.8 and PSB-AR-9.9.

As the applied load increases, the vertical displacement increases gradually but as it is observed from Fig. 3, increasing prestressing force significantly reduces the deflection at the ultimate stage. For normalized prestress factor α from 0.4 to 1.0, the bridge collapse at small deflection due to premature decompression (Fig. 5), and the damage were restricted to the top flange of the 8th segment and 9th segment for PSB-AR-18.4 and PSB-AR-15.6 but in the mid-span for other two PCSB model.

321 The DFE model of PCSB attain decompression state briefly upon application of monotonic loading
322 when $\alpha = 1.7$, but still, the numerical model could sustain larger deformation before failure. It may
323 be due to secondary effects provided by the unbonded tendons which could stabilise the structure and
324 prevent it from deflecting uncontrollably. From Fig. 4, the assessed value for the ratio of mid-span
325 deflection to the length of the segmental bridge model are $15.8e^{-3}$, $18.7e^{-3}$, $13.1e^{-3,}$ and $14.7e^{-3}$ for
326 PSB-AR-18.4, PSB-AR-15.6, PSB-AR-12.8, and PSB-AR-9.9, respectively.

327

328 **Table 4**. Performance of PCSBs at DC and PL states.

Model	α_i	Decompression (DC)		Peak load (PL)		Strain in T5L tendon	Tendon slip at deviator 2
		Δ_{DC} (mm)	M_{DC} (MN·m)	Δ_{PL} (mm)	M_{PL} (MN·m)	ε_α	δ_α^{slip} (mm)
PSB-AR-18.4	0.4	0.00	0.00	48.87	3.63	0.000	0.00
	1.0	0.00	0.00	266.03	13.62	0.0009	5.19
	1.7	1.30	0.23	698.30	35.10	0.0027	20.03
	2.6	17.93	11.74	561.73	40.22	0.0020	17.49
	3.5	35.93	24.20	480.47	48.41	0.0016	15.51
	4.4	52.58	36.49	351.75	58.15	0.0011	12.79
	5.3	75.01	50.87	245.20	63.39	0.0005	6.17
PSB-AR-15.6	0.6	0.00	0.00	250.26	24.22	0.0015	6.8
	1.0	0.00	0.00	618.57	57.27	0.0032	18.4
	1.7	0.37	0.06	679.21	62.86	0.0029	21.2
	2.4	8.30	7.95	671.69	71.63	0.0024	21.3
	3.6	23.24	22.62	511.82	71.44	0.0011	17.8
	4.4	31.30	30.85	351.50	66.11	0.0002	10.9
	4.8	36.69	35.62	44.26	38.44	0.000	0.7
PSB-AR-12.8	0.6	0.34	0.07	290.65	32.00	0.0021	16.2
	1.0	1.79	0.24	342.90	38.82	0.0024	15.07
	1.7	1.33	0.67	399.50	45.32	0.0029	22.15
	2.8	7.77	10.22	390.89	53.31	0.0026	21.84
	3.8	13.32	19.26	352.44	57.83	0.0023	20.37
	4.4	16.48	24.50	245.21	50.60	0.0016	15.39
	4.8	19.16	27.45	182.82	46.89	0.0011	11.93
PSB-AR-9.9	0.6	1.25	0.27	147.56	34.37	0.0017	13.7
	1.0	1.84	0.47	187.82	44.56	0.0022	16.71
	1.7	1.25	1.24	351.29	86.30	0.0042	30.93
	2.8	2.95	7.06	293.60	77.47	0.0034	24.6
	3.8	4.87	15.75	237.13	74.51	0.0026	20.39
	4.4	6.38	21.72	198.11	70.22	0.0022	17.83
	4.8	7.18	24.82	115.53	53.62	0.0013	10.98

(a)

(b)

(c)

(d)
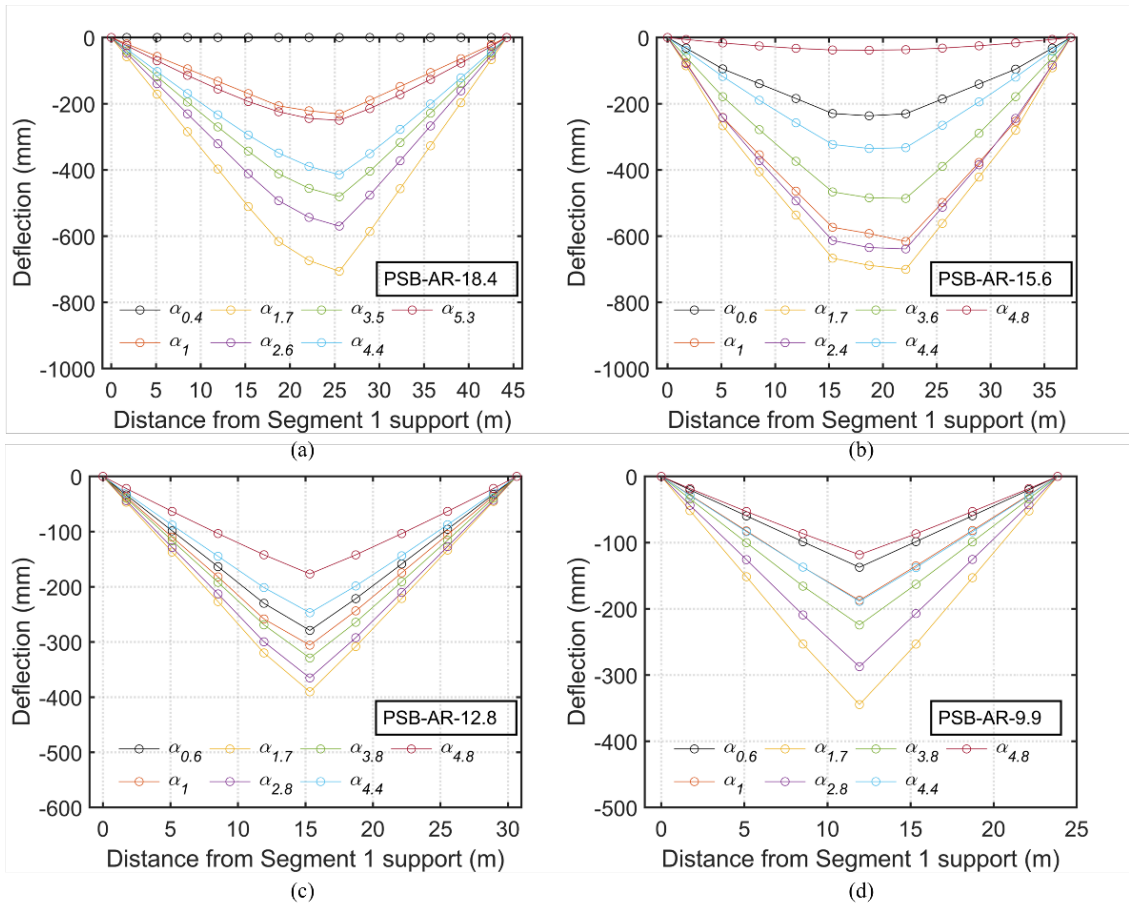
Fig. 4. Deflection profiles at Peak Load (PL) stage.

(a)

(b)

(c)

(d)
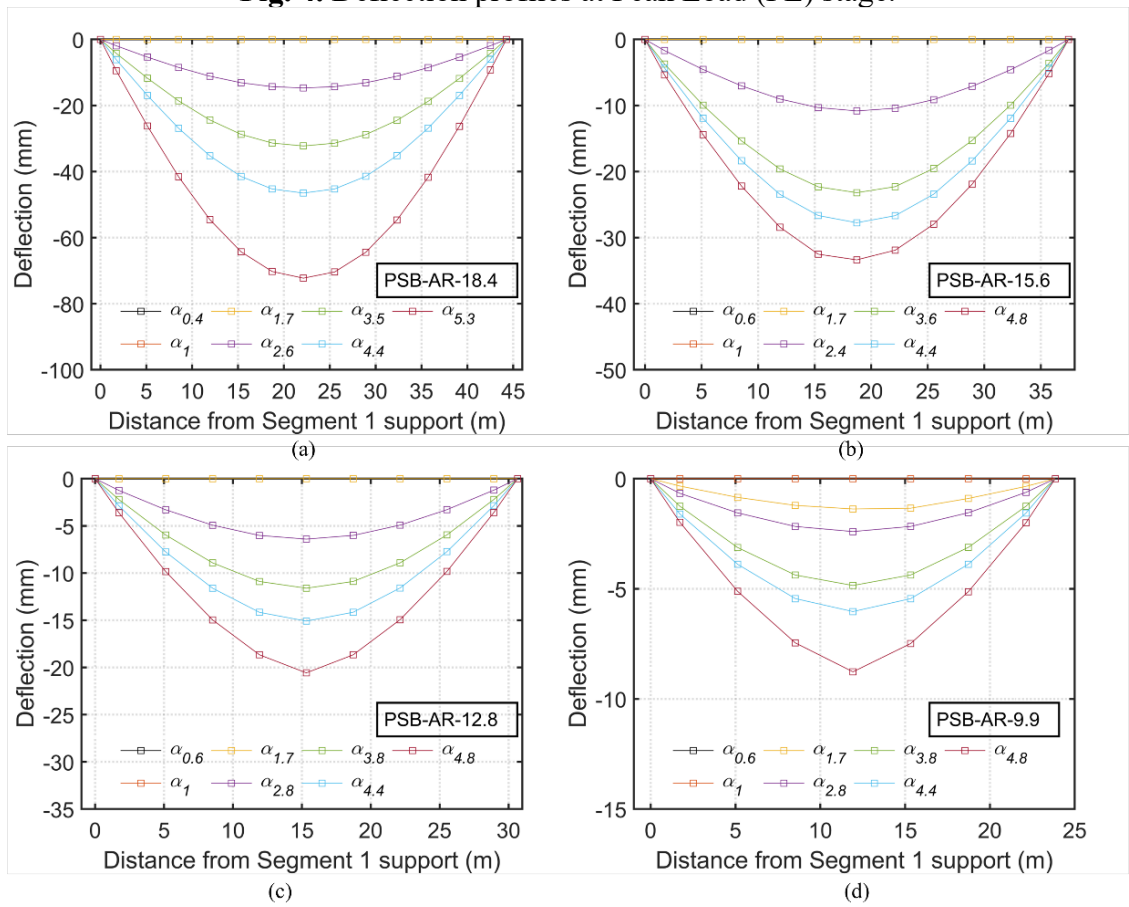
Fig. 5. Deflection profiles at decompression (DC) stage.

333 ### 3.3 *Influence of prestressing force and aspect ratio*

334 #### 3.3.1 *Deformation and mid-span moment characteristics*

335   The PSCBs models have varied span length but have the same depth of the segment, cross-
336 section, and material properties and thus have aspect ratios of 18.44, 15.60, 12.77, and 9.94 for PSB-
337 AR-18.4, PSB-AR-15.6, PSB-AR-12.8, and PSB-AR-9.9 respectively. The relation between
338 prestressing force, deflection, and mid-span moments are shown Figs. 6(a)-(d). It is observed from
339 Figs. 3 (b) & (d) that deflection and moment resistance shows a linear relationship with a positive
340 slope when the normalized prestress factor increases from 1.7 to 4.4 at the DC stage. The models
341 which lie in the category of $\alpha < 1.7$ and $\alpha > 4.4$ have low load-carrying capacity due to
342 decompression under the self-weight, as the presence of very little prestress force unable to resist the
343 self-weight. Where, in case of higher α value (4.8 & 5.3), the structure collapse soon exhibiting
344 brittle failure due to large compressive force by prestressing tendon. Thus, the figure is divided into
345 three zones i.e., premature decompression zone (PDZ with $\alpha = 0.4 - 1.7$), normal prestress zone
346 (NPZ with $\alpha = 1.7 - 4.4$), and over-prestress zone (OPZ with $\alpha = 4.4 - 5.3$).
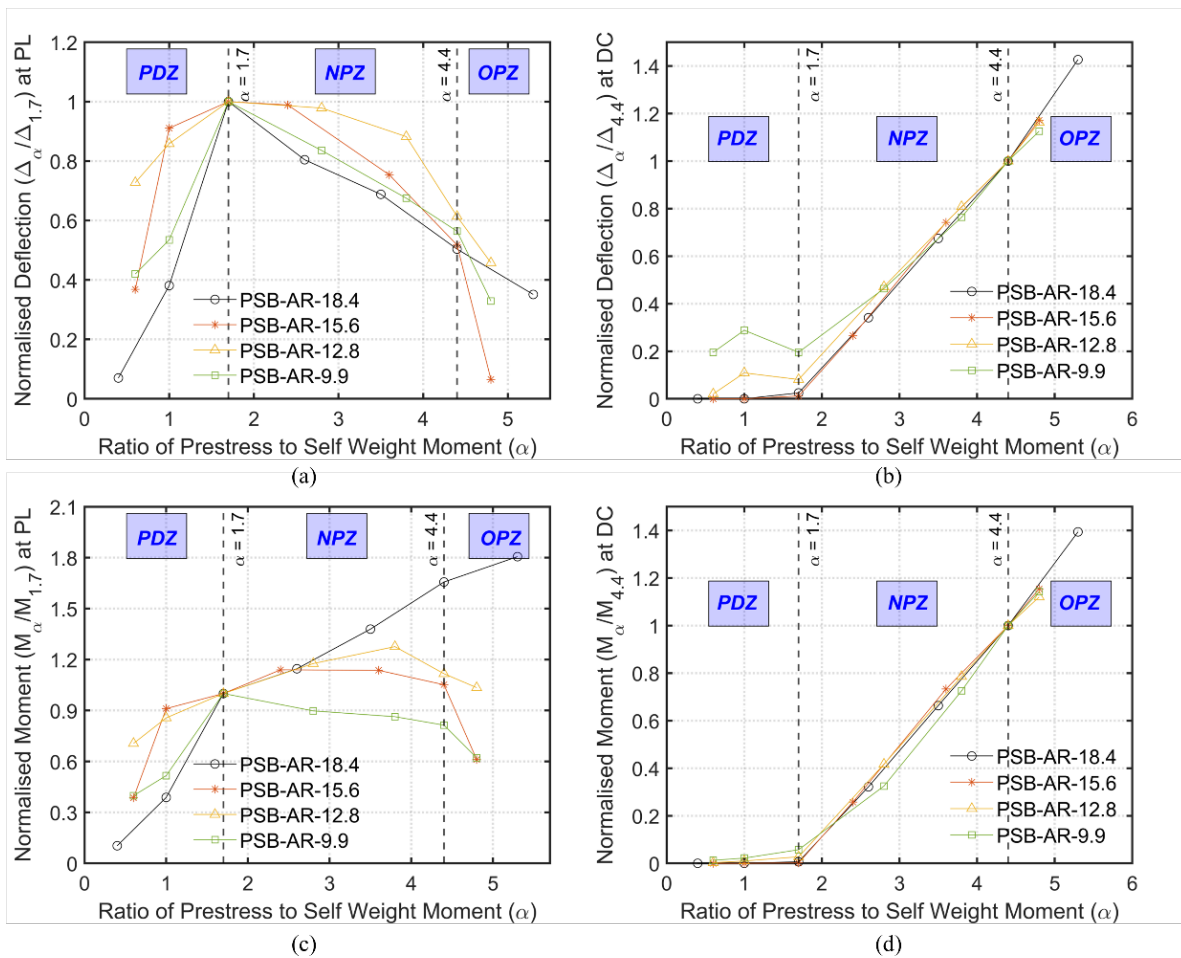
347

348   **Fig. 6.** Relationship between prestressing forces, deflections, and mid-span moments.

349

On contrary, the deflection at the ultimate stage shows linearly related to the prestressing force with a negative slope as normalized prestress factor increase. Fig. 6(a) shows that aspect ratio affects the relationship between deformation and prestress force. As the aspect ratio increases from 9.94 to 18.44, the rate of decrease of the deflection with prestress becomes higher and shows an approximately linear relationship with a gradual slope. Fig. 6(c) shows the complex relationship between the moment-resisting capacities of PCSBs at the PL stage and increased prestress due to the variation in the span-depth ratio. For model with L/d varies from 9.94 to 15.60, the ultimate moment shows nearly constant relation with prestress due to small variations of the moment but for PSB-AR-18.4, it shows linearly related to the increasing prestress force with positive gradient.

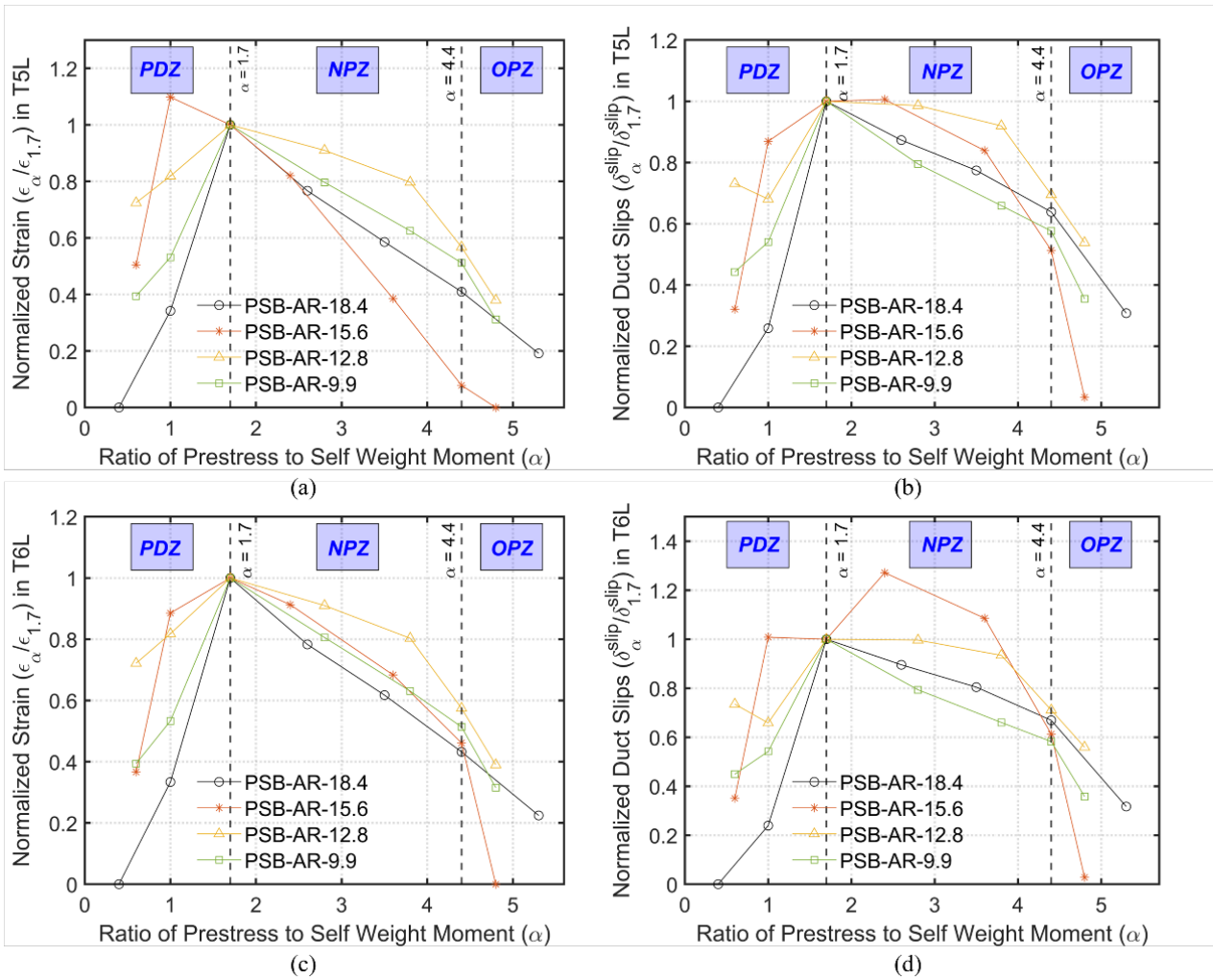### 3.3.2   Variations in tendon strains and duct slip

Fig. 9 shows the relationship between prestressing forces, tendon strain, and duct slip of two tendons T5 (long) and T6 (short) at the ultimate state. It is observed from Figs. 9(a) & (b) that the tendon strain in all the bridge model increase in the pre-mature decompression zone as the prestressing level increases and decrease when the normalized prestress factor is above 1.7, except for PSB-AR-15.6 (in T5). The increase in the tendon strain is due to the deflection of the bridge under vertical loads. Thus, the trends of strains have close affinities to the deflection curves.

It is seen from the curves between the tendons strain and prestressing force exhibit an approximately linear relation with negative slope regardless of the span length of the bridge model. However, there is a slight variation in the case of bridge PSB-AR-12.8 in prestress zone. The T5 tendon is placed end to end of the span and having a trapezoidal profile. The maximum value of strain ε_α in the T5 tendon that occurred at $\alpha = 1.7$, were 0.0027, 0.0029, and 0.0042 respectively for PSB-AR-18.4, PSB-AR-12.8, and PSB-AR-9.9 but the maximum strain recorded for PSB-AR-15.6 is 0.0032 at $\alpha = 1.0$. The T6 tendon is the shortest and has a straight profile placed between the 4th and 11th segments. Similarly, the maximum strain was recorded at $\alpha = 1.7$ for all models. The value $\varepsilon_{1.7} = 0.005$ is constant for PSB-AR-18.4, PSB-AR-15.6 and PSB-AR-12.8 except for PSB-AR-9.9, where the maximum recorded strain is slightly higher i.e., $\varepsilon_{1.7} = 0.0054$. Therefore, the tensile strain in the trapezoidal profile tendon is higher in the shorter span model at a given prestress force, increasing the steepness of the slope of the curve as the span length increases. For the straight profile, the steepness of the slopes is similar to the first three models with the brief discrepancy in the shorter model within the prestress zone.

Fig. 7. Relationship between prestressing forces, tendon strains, and duct slips.

There are also similarities in trends between the duct slip in T5 Fig. 7(b) and the ultimate deflections, and notably between the tendons (T5&T6) but differences can be observed in the case of PSB-AR-15.6 in Fig. 7(d). The tendons suffer exceedingly small duct slip before the collapse for normalized prestress factor below 1.7 and above 4.4 because of early failure of models due to premature decompression under self-weight of the bridge in the earlier case and suffer early crushing of concrete under high compressive stress due to large prestressing force in the later. The tendons are unbonded and only connected to the deviators to achieve trapezoidal profile and anchorage for the short tendons at the end. Thus, allow the tendons to slip away from the deviator. The strand slip at deviator 2 was recorded. The maximum value of duct slip δ_α^{slip} in the T5 tendon that occurred at $\alpha = 1.7$, were 20.03 mm, 21.20 mm, and 22.15mm respectively for PSB-AR-18.4, PSB-AR-15.6, and PSB-AR-12.8 and the largest strain of value 30.93 mm is observed in PSB-AR-9.9. Similarly, the maximum duct slips for T6 tendons were 15.47 mm, 18.36 mm, and 27.18 mm respectively for PSB-AR-18.4, PSB-AR-12.8, and PSB-AR-9.9 but the maximum slip recorded for PSB-AR-15.6 is 21.97 mm at $\alpha = 2.4$. From Fig. 7(d), it is observed that the slope of the curve for PSB-AR-12.8 is flat since

398   the changes are minute in slip value in the normal prestress zone. Therefore, PSB-AR-18.4 and PSB-

399   AR-9.9 are the only models that exhibit the trends.

400   *3.3.3   Comparison of change in stress and total tendon stress*

401   The stress increase in the tendons is a significant parameter for understanding the performance

402   of the unbonded tendons at the ultimate limit state (ULS). The assumption of the plane section

403   remains plane is not valid for segmental bridges with unbonded tendons, as the movement of the

404   tendons is not constrained in the beam's longitudinal direction except for the anchorage points. The

405   general form recommend by the existing design code (AASHTO LRFD [42], EC2 [32], and ACI318-

406   19 [43]) for calculation the total stress (f_{ps}) of unbonded tendons at the ULS is given as:

407
$$f_{ps} = f_{pe} + \Delta f_{se} \leq f_{py} \tag{12}$$

408   where, f_{pe} is the effective prestress applied to the tendon, Δf_{se} is the increase in stress and f_{py} is the

409   tendons' yield strength. The equation recommended by the existing design code for calculation of the

410   increase in stress (Δf_{se}) is given as:

411
$$\Delta f_{se} = 6205 \left(\frac{d_p - c}{l_e}\right) \text{MPa} \qquad \text{(AASHTO LRFD)} \tag{13a}$$

412
$$\Delta f_{se} = 100 \text{ MPa} \qquad \text{(EC2)} \tag{13b}$$

413
$$\Delta f_{se} = \min\left[70 + f_c^{'}/(100\rho_p),\ \ 420\right] \text{MPa} \ \text{ for } l_n/h \leq 35 \text{ (ACI318-19)} \tag{13c}$$

414
$$\Delta f_{se} = \min\left[70 + f_c^{'}/(300\rho_p),\ \ 210\right] \text{MPa} \ \text{ for } l_n/h > 35 \text{ (ACI318-19)} \tag{13d}$$

415   where, d_p = distance between the centroid of the tendons and extreme compression fiber; ρ_p is

416   prestressing ratio; c = depth of the compressive zone; l_e = effective length of the tendon; l_n = clear

417   span length; and h = depth of the concrete segment. Eqs. 11(c) & 11(d) are permitted only for $f_{se} \geq$

418    $0.5 f_{pu}$. The f_{ps} determined by solving Eq. 11(a) and c simultaneously with the equilibrium condition.

419   The variation in stress change (left axis) and ultimate stress (right axis) in the short tendon (T6)

420   under different prestress levels is shown in Fig. 8. As discussed above, tendon stress is a significant

421   attribute in assessing the performance of the unbonded tendons at the ultimate limit state (ULS). The

422   prediction of an increase in stress as per the ACI318-19 [43] and AASHTO LRFD [42] are in good

423   agreement with the numerical result in each case at $\alpha = 4.4$, but the corresponsding effective

424   prestress force differ i.e., $0.624 f_{pu}, 0.449 f_{pu}, 0.306 f_{pu}$ and $0.212 f_{pu}$ for PSB-AR-18.4, PSB-AR-

425   15.6, PSB-AR-12.8, and PSB-AR-9.9, respectively. In OPZ, the segmental bridge with aspect ratio

426   18.4 and 15.6 provide higher value of stress increment in comparison with both the code provision.

427   Whereas, PSB-AR-12.8 agrees only with the AASHTO prediction and PSB-AR-9.9 shows good

428   agreement only with the ACI specification. A similar agreement can be observed in PDZ with an

exception for PSB-AR-15.6. In NPZ, ACI318-14 produce conservative results for all the box-girder segmental bridge numerical model and similar predictions showed by AASHTO LRFD. While the EC2 [32] underestimate the stress change for all the models except for PSB-AR-15.6 ($at\ \alpha = 4.8$). However, the change in tendon stress is dependent on normalized prestress factor and also associated with the aspect ratio of the structure is evident, but both the design codes ignore such dependency. It is observed from Fig. 8(a) that the ultimate tendon stress at BF is more stable in comparison to stress change. Hence, constant ultimate stress would be more appropriate for assessing the ULS behaviour of externally prestressed PCSBs rather than constant stress change.
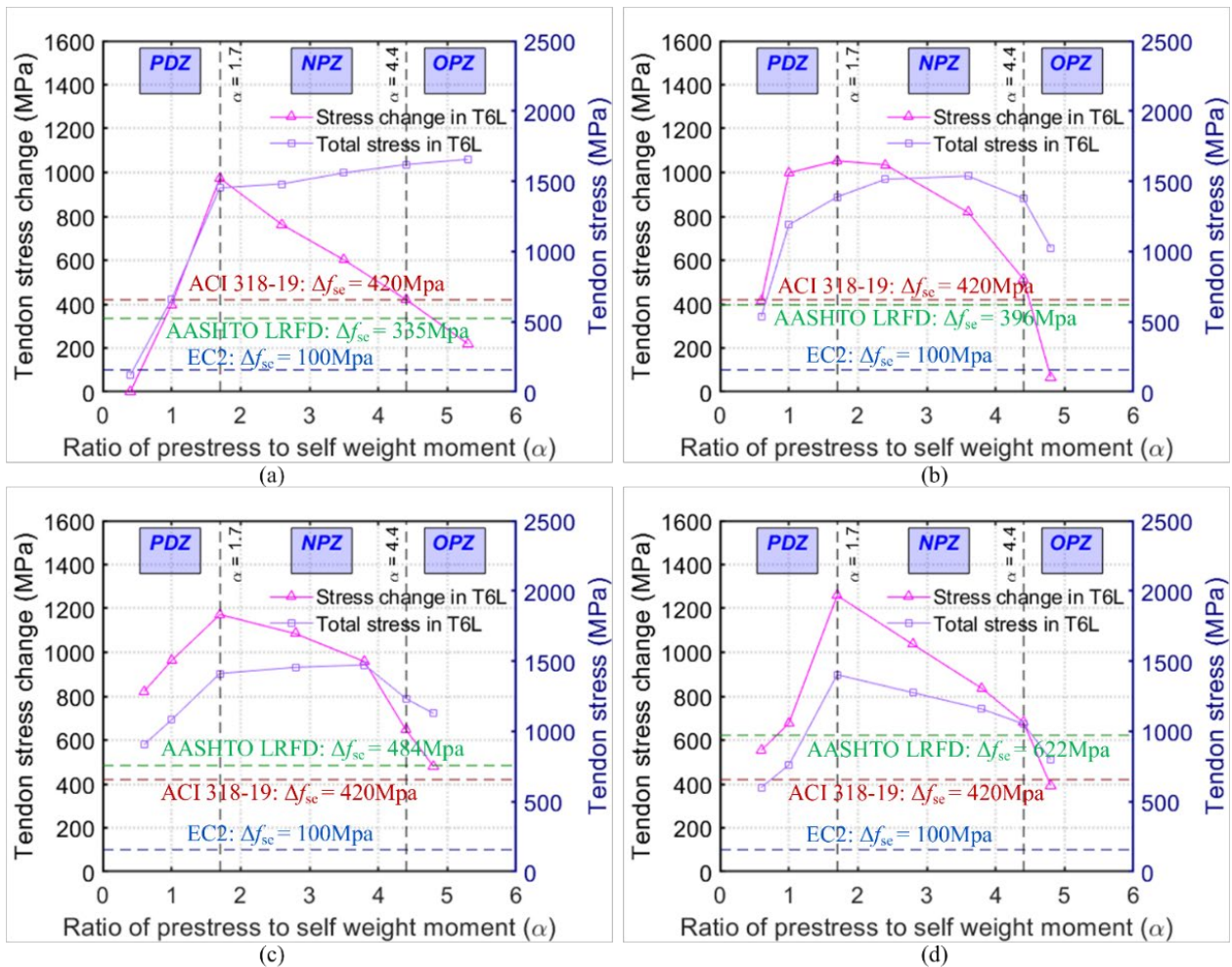
Fig. 8. Effects of the variations in effective prestress on stress changes and the maximum tension stress at BF with different aspect ratio (a) PSB-AR-18.4, (b) PSB-AR-15.6, (c) PSB-AR-12.8, and (d) PSB-AR-9.9.
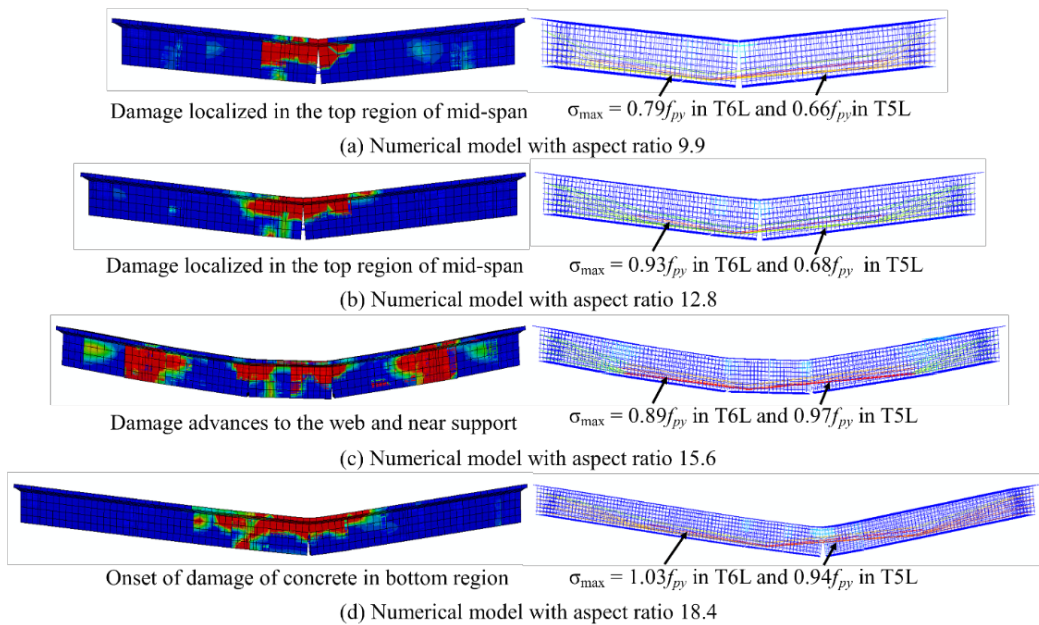
3.4 *Failure modes*

Initially, the segmental prestress bridge behaves as an integral structure. As the structure is subjected to vertical load, the decompression of the bridge occurred. On further increase in load, a critical joint opened, and ultimately, the bridge collapsed. In this study, all the models are subjected to brittle failure. The failure modes of all the generated numerical models with different aspect ratio for normal prestress zone is shown in Fig. 9. It is observed that for the model with aspect ratios 12.8 and 9.9 subject to damage which is constrained to the top region in the mid-span of the structure. For PSB-AR-15.6, the damage advances to the web region and visible near the support and distributed over a large portion. For models with the highest aspect ratio, the damage of concrete in the bottom region is visible at the ultimate state. The damage proliferates over a wide area of the top region of mid-span also with the joint opening at the right of the centerline of the structure.

The incurred damage, which is depicted by the equivalent plastic strain (PEEQ), at the BF stage (just before collapse) of PSB-AR-18.4 in the different prestressing zone is shown in Fig. 10. In PDZ, the bridge endures very limited deflection before the collapse, and the damage was restricted within the top flange of the 8th segment and 9th segment due to the decompression in the early loading stage. Similarly, the bridge failed due to the crushing of concrete in the top zone in NPZ but the damage distribution is large. In OPZ such as $\alpha = 5.3$ $(1.2f_{pu})$ the failure occurs due to damage of concrete in both top and bottom zone due to high compressive stress produce by prestressing force. Whereas max principal stress in the tendon is $0.74f_{py}$, $0.94f_{py}$ and $1.03f_{py}$ in PDZ, NPZ, and OPZ, respectively.
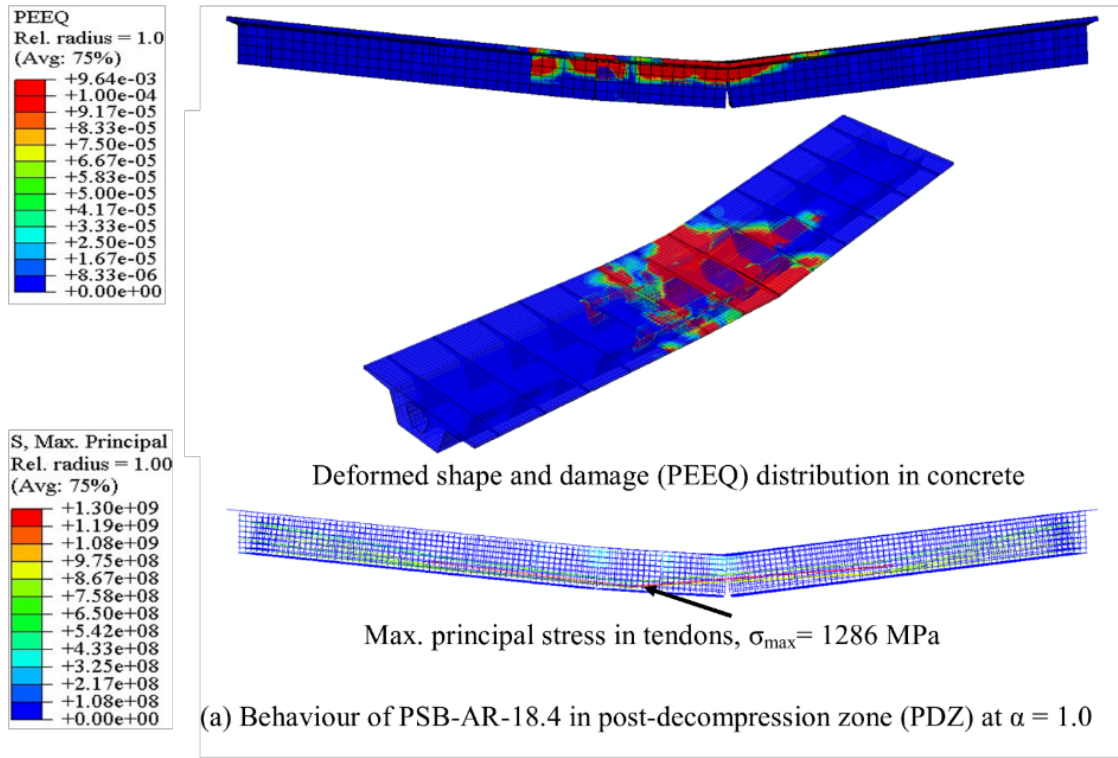

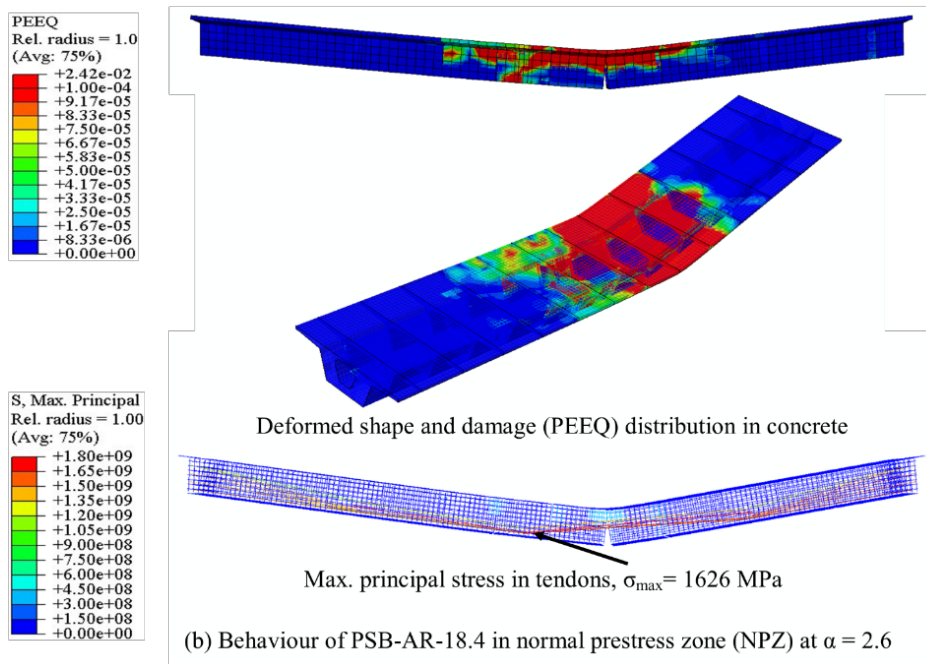Damage localized in the top region of mid-span $\sigma_{max} = 0.79f_{py}$ in T6L and $0.66f_{py}$ in T5L

(a) Numerical model with aspect ratio 9.9

Damage localized in the top region of mid-span $\sigma_{max} = 0.93f_{py}$ in T6L and $0.68f_{py}$ in T5L

(b) Numerical model with aspect ratio 12.8

Damage advances to the web and near support $\sigma_{max} = 0.89f_{py}$ in T6L and $0.97f_{py}$ in T5L

(c) Numerical model with aspect ratio 15.6

Onset of damage of concrete in bottom region $\sigma_{max} = 1.03f_{py}$ in T6L and $0.94f_{py}$ in T5L

(d) Numerical model with aspect ratio 18.4

Fig. 9. Failure modes at NPZ (α=2.6) for models with different aspect ratios.

468

Deformed shape and damage (PEEQ) distribution in concrete

Max. principal stress in tendons, σ_{max}= 1286 MPa

(a) Behaviour of PSB-AR-18.4 in post-decompression zone (PDZ) at $\alpha = 1.0$

469

Deformed shape and damage (PEEQ) distribution in concrete

Max. principal stress in tendons, σ_{max}= 1626 MPa

(b) Behaviour of PSB-AR-18.4 in normal prestress zone (NPZ) at $\alpha = 2.6$

470   **Fig. 10.** Failure modes at PDZ (α=1.0), NPZ (α=2.6), OPZ (α=4.8) for models with the same aspect
471   ratio but different normalized prestress factor (α).
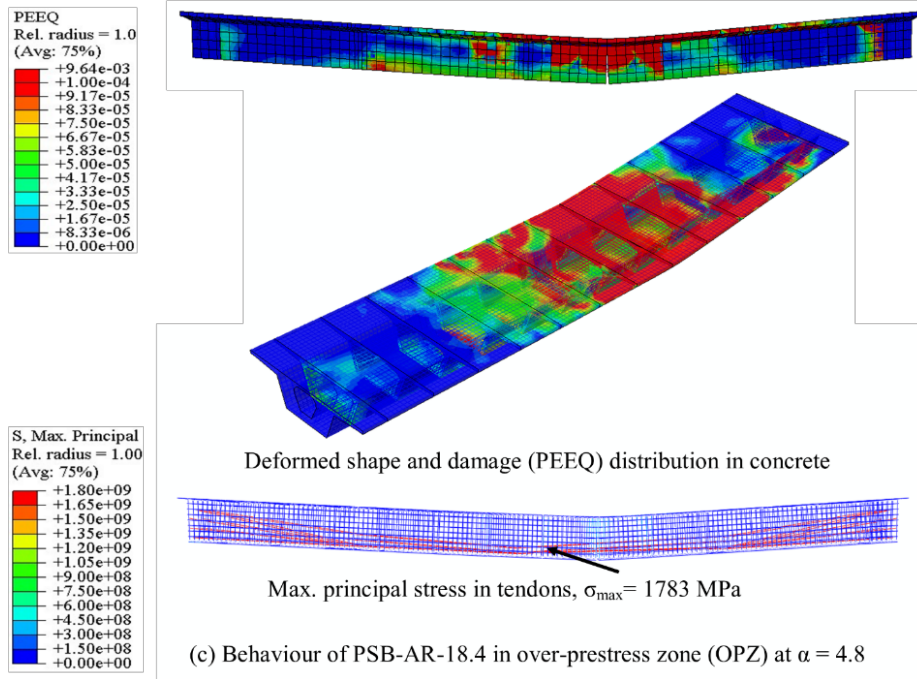
472

Fig. 10. Failure modes at PDZ (α=1.0), NPZ (α=2.6), OPZ (α=4.8) for models with the same aspect ratio but different normalized prestress factor (α) (cont'd).

4. Response Surface Analysis of Tendon Stress at ULS

4.1 *First-order fitting*

In Figs. 11(a-d), the design codes [32,42,43] produces conservative results when the structure is in NPZ. Since the stress change in the unbonded tendons is greatly affected by both prestress level and aspect ratio and crucially important in the prediction of tendon stress at the ultimate limit state, the objective is to provide an accurate expression for rational evaluation of the stress in unbonded tendons, specifically, for box girder segmental type structures. For this purpose, Response Surface Methodology (RSM), a well-known statistical tool [44], is utilized to form the mathematical relationship between the independent variable (normalized prestress factor (α), aspect ratio (L/d)) and dependent variables (stress change (Δf_{se}), total stress (f_{ps})). Initially, the statistical analysis carried out with lower-order linear model to identify the which parameter is more influential on the response. The first-order linear model represents relationship between independent variables and the response is shown by Eq. (12).

$$y = \lambda_0 + \lambda_1 x_1 \tag{14}$$

where y is the estimated response, λ_0 is the y-intercept for which $x_1 = 0$, whereas λ_1 is the coefficient for the independent variable (x_1). The independent variables x_i considered here are the normalized prestress factor α and the aspect ratio L/d. The results of the linear model are given in Fig. 11 along

with the relationship expressed in actual values of the regression coefficients. However, the very small values of R^2 exhibit the mediocre prediction by the linear model and thus, the expression is inadequate to conclude the dependency of the response variable on both independent variables.

## 4.2 *High-order fitting*

Some recent studies indicate that the aspect ratio and effective prestress level significantly affect the tendon stress at the ultimate stage, but the effect of aspect ratio is profound [8,9]. Thus, the influence of aspect ratio and prestress level on response parameter are of particular interest. For this purpose, after initial fit, a cubic response surface including both the interaction term is then fitted to the numerical data. The functional form of the polynomial model can be expressed as

$$y = \lambda_0 + \lambda_1 \frac{L}{d} + \lambda_2 \alpha + \lambda_{12} \alpha \frac{L}{d} + \lambda_{11} \left(\frac{L}{d}\right)^2 + \lambda_{22} \alpha^2 + \lambda_{111} \left(\frac{L}{d}\right)^3 + \lambda_{112} \alpha \left(\frac{L}{d}\right)^2 + \lambda_{122} \alpha^2 \frac{L}{d} \quad (15)$$

where $\lambda_0, \lambda_i, \lambda_{ij}, \lambda_{ijk}$ with i, j, k = 1, 2 are the fitting coefficients for the zero, first, second, and third-order terms of the response $y = \Delta f_{se}$ or f_{ps} with independent variables L/d and α. However, in Eq. (15), the variable of aspect ratio is provided with a higher degree than normalized prestress factor variable to accord well with the conclusion of the aforementioned study.
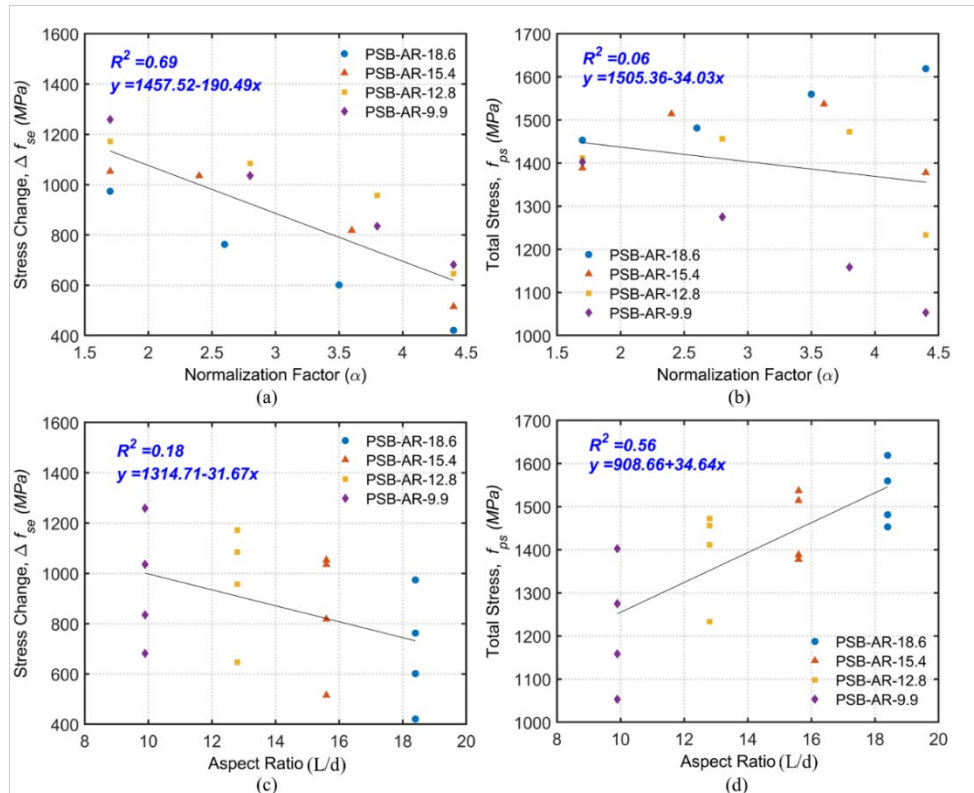
Fig. 11. Influence of the normalized prestress factor α and aspect ratio L/d on stress change Δf_{se} and total stress f_{ps}.

The calculated λ coefficient for the terms in the cubic response surface is given in Table 5. The response surface obtained for corresponding stress change and total stress using the polynomial model are presented in Fig. 12. For both of the response surfaces, the goodness-of-fit R^2 values of the regression were 0.97 and 0.92, respectively. Therefore, it is evident that the established model is adequate and capable of predicting the stress change and total stress of unbonded tendons in PCSBs at ultimate state. As shown in Fig 13(a), the stress change in tendon decreases with an increase in the normalized prestress factor (α) and aspect ratio (L/d) but more specifically, providing higher effective prestress force is more beneficial for limiting the stress change in the unbonded tendon. This attribute to the fact that the increase in normalized prestress factor not only decreases the stress change in the tendon but also greatly enhances the load-carrying capacity.

Compare to the stress change response, the aspect ratio has a limited influence on the total stress response when the normalized prestress factor has a lower value, as shown in Fig. 12(b). These observations can be further confirmed by the obtained stress value with the variation in aspect ratio shown in Fig. 7, though, aspect ratio highly influences the total stress in the unbonded tendon when the normalized prestress factor is higher. In considering the influence of normalized prestress factor, it is also observed that the polynomial model produces a uniform response surface for the models with a high aspect ratio in contrast to the lower aspect ratio models.

Table 5. The coefficients in response surface analysis.

Coefficient	Values	
	Stress change (Δf_{se})	Total stress (f_{ps})
λ_0	968.3	1479
λ_1	-173.9	54.42
λ_2	-202.6	-31.89
λ_{12}	2.301	77.3
λ_{11}	-58.99	-29.03
λ_{22}	-49.46	-50.8
λ_{111}	30.65	30.23
λ_{112}^	-13.59	-4.206
λ_{122}	9.763	9.351

^ Subscripts of λ_{ijk} with i, j, k = 1, 2 represent orders of the independent variables: (1) = L/d and (2) = α. For instance, λ_{112} is the coefficient of (1)×(1)×(2) = $(L/d)^2 \alpha$.
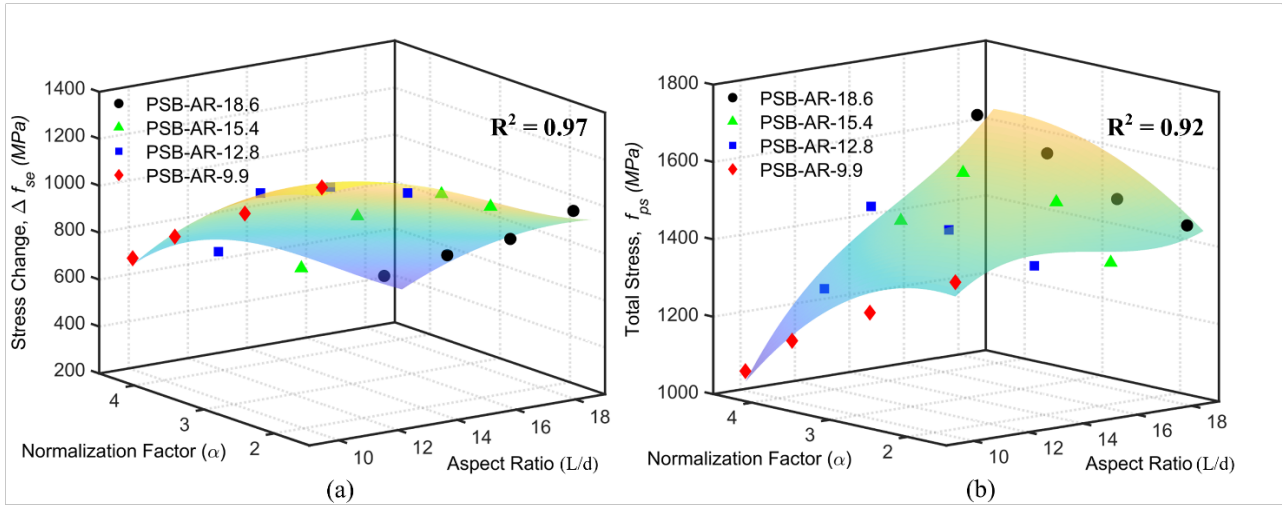
Fig. 12. Response surface showing the relationship between normalized prestress factor α and aspect ratio L/d w.r.t. (a) stress change Δf_{se} and (b) total stress f_{ps}.

4.3   *Engineering implications*

In practices, the geometry or aspect ratio (L/d) of bridges is fixed, but the normalized prestress factor (α) would be relatively less certain as a result of the unpredicted prestress loss or grain as discussed above. As shown in the above analysis results both variables have significant effects on the tendon stress change and the total tendon stress that in turn govern the failure modes and deformation capacities at the ULS. It was shown in the above response surface analysis (Fig. 12) that the total tendon stress at ULS is less sensitive to the change of α for PCSBs with a high aspect ratio (L/d). The moment capacity (Fig. 6(c)) of high aspect ratio PSB-AR-18.6 increase with increasing α, while the total tendon stress at ULS remains relatively stable (Fig. 12). However, when the aspect ratios of PCSBs decrease, the total stress at ULS drops quite obviously and the moment capacities would decrease with increasing α after α has reached a specific value $\alpha_{crit} = 3.8, \ 3.6, \text{and } 1.7$ for $L/d = 15.4, 12.8, \text{and } 9.9$ respectively. This could be attributed to the increasing interacting shear-flexural action (Fig. 9). In particular, for $L/d = 9.9$, the $\alpha_{crit} = 1.7$ is the boundary between the NPZ (normal prestress zone) and PDZ (premature decompression zone). Since the deflection at peak loads (Fig. 6(a)) uniformly decreases with increasing α regardless of the aspect ratio, high prestress on PCSBs with low aspect ratios may have no advantages in terms of the deflection and moment capacities. Meanwhile, the high prestress on flexural-controlled PCSBs can enhance the moment capacity but on the other hand, reduce the deflection capacity.

5. Conclusions

The numerical models with varied span lengths were developed using the proposed DFEM and are used to study the nonlinear behaviour of PCSB with dry-shear keys and externally unbonded tendons. The influence of aspect ratio and different prestress levels on tendon stress and the assessment of stress increment at ultimate limit state with various code provisions are also studied. The following conclusion was drawn based on the analysis results:

1. Increasing the aspect ratio significantly reduces the bridge strength and stress change in the tendon.
2. All the examined design codes produce conservative results for the unbonded tendon stress at the ultimate state in the normal prestress zone (NPZ), however, ACI318-19 can predict better stress changes in the OPZ. EC2 yielded highly conservative stress change prediction in all zones.
3. Even though the trends of stress change in the tendon are similar in all the models, but the tendon stress at the ultimate state becomes more stable as the prestress level increases for the models with a higher aspect ratio.
4. The first-order linear model shows a lower degree of correlation. Thus, establish the dependency of the response variable on both independent variables. Although, the response model achieved mediocre prediction with 69% of the variability in stress change and 56% of the variability in total stress when considering normalized prestress factor and aspect ratio, respectively.
5. The 3rd order two-variable response surface analysis shows a significant correlation between the independent and response variable with high R^2 values (> 0.92). In general, the model predicts lower stress change for higher normalized prestress factor and aspect ratio, but an inverse correlation is observed in the case of total stress.
6. The aspect ratio interaction with the response parameter was found to be crucial and shows a non-linear correlation. Whereas, the interaction is close to linear between normalized prestress factor and stress change. However, the effect of aspect ratio is not profound on total stress when the normalised prestress factor is lower.

References

[1]   LinW, YodaT. Reinforced and Prestressed Concrete Bridges. Bridg. Eng., Elsevier; 2017, p. 97–110. https://doi.org/10.1016/B978-0-12-804432-2.00006-2.

[2]   AhmedGH, AzizOQ. Stresses, deformations and damages of various joints in precast concrete segmental box girder bridges subjected to direct shear loading. Eng Struct 2020;206:110151. https://doi.org/10.1016/j.engstruct.2019.110151.

[3]   SaibabuS, SrinivasV, SasmalS, LakshmananN, IyerNR. Performance evaluation of dry and epoxy jointed segmental prestressed box girders under monotonic and cyclic loading. Constr Build Mater 2013;38:931–40. https://doi.org/10.1016/j.conbuildmat.2012.09.068.

[4]   BuZY, WuWY. Inter shear transfer of unbonded prestressing precast segmental bridge column dry joints. Eng Struct 2018;154:52–65. https://doi.org/10.1016/j.engstruct.2017.10.048.

[5]   AhmedGH, AzizOQ. Shear behavior of dry and epoxied joints in precast concrete segmental box girder bridges under direct shear loading. Eng Struct 2019;182:89–100. https://doi.org/10.1016/j.engstruct.2018.12.070.

[6]   RombachG, SpeckerA, ZhouX, MickleboroughN, LiZ. Shear strength of joints in precast concrete segmental bridges. ACI Struct J 2005;102:901–4.

[7]   YuanA, HeY, DaiH, ChengL. Experimental study of precast segmental bridge box girders with external unbonded and internal bonded posttensioning under monotonic vertical loading. J Bridg Eng 2015;20:1–12. https://doi.org/10.1061/(ASCE)BE.1943-5592.0000663.

[8]   LeTD, PhamTM, HaoH, HaoY. Flexural behaviour of precast segmental concrete beams internally prestressed with unbonded CFRP tendons under four-point loading. Eng Struct 2018;168:371–83. https://doi.org/10.1016/j.engstruct.2018.04.068.

[9]   LeTD, PhamTM, HaoH. Numerical study on the flexural performance of precast segmental concrete beams with unbonded internal steel tendons. Constr Build Mater 2020;248:118362. https://doi.org/10.1016/j.conbuildmat.2020.118362.

[10]   HurstMK. Prestressed Concrete Design. 2nd ed. Taylor & Francis Group, New York; 2017.

[11]   VSL. External Post-Tensioning: Design Considerations VSL External Tendons Examples from Practice. VSL International LTD.; 1992.

[12]   WeiherH, ZilchK. Condition of post-tensioned concrete bridges - assessment of the German stock by a spot survey of damages. Proc. First Int. Conf. Adv. Bridg. Eng. London, UK, 2006, p. 26–8.

616 [13] SchupackM, SuarezMG. Some Recent Corrosion Embrittlement Failures of Prestressing
617 Systems in the United States. PCI J 1982;27:38–55.

618 [14] ACl-ASCE Committee 423. Guide to Estimating Prestress Loss. Farmington Hills, MI: ACI;
619 2016.

620 [15] AparicioAC, RamosG, CasasJR. Testing of externally prestressed concrete beams. Eng Struct
621 2002;24:73–84. https://doi.org/10.1016/S0141-0296(01)00062-1.

622 [16] TurmoJ, RamosG, AparicioAC. FEM study on the structural behaviour of segmental concrete
623 bridges with unbonded prestressing and dry joints: Simply supported bridges. Eng Struct
624 2005;27:1652–61. https://doi.org/10.1016/j.engstruct.2005.04.011.

625 [17] TurmoJ, RamosG, AparicioAC. FEM modelling of unbonded post-tensioned segmental beams
626 with dry joints. Eng Struct 2006;28:1852–63. https://doi.org/10.1016/j.engstruct.2006.03.028.

627 [18] TurmoJ, RamosG, AparicioÁC. Shear behavior of unbonded post-tensioned segmental beams
628 with dry joints. ACI Struct J 2006;103:409–17. https://doi.org/10.14359/15319.

629 [19] LiG, YangD, LeiY. Combined Shear and Bending Behavior of Joints in Precast Concrete
630 Segmental Beams with External Tendons. J Bridg Eng 2013;18:1042–52.
631 https://doi.org/10.1061/(asce)be.1943-5592.0000453.

632 [20] LiG, ZhangC, NiuC. Experimental Study on Shear Behavior in Negative Moment Regions of
633 Segmental Externally Prestressed Concrete Continuous Beams. J Bridg Eng 2013;18:328–38.
634 https://doi.org/10.1061/(asce)be.1943-5592.0000351.

635 [21] AlgorafiMA, AliAAA, OthmanI, JaafarMS, AnwarMP. Experimental study of externally
636 prestressed segmental beam under torsion. Eng Struct 2010;32:3528–38.
637 https://doi.org/10.1016/j.engstruct.2010.07.021.

638 [22] YuanA, DaiH, SunD, CaiJ. Behaviors of segmental concrete box beams with internal tendons
639 and external tendons under bending. Eng Struct 2013;48:623–34.
640 https://doi.org/10.1016/j.engstruct.2012.09.005.

641 [23] JiangH, CaoQ, LiuA, WangT, QiuY. Flexural behavior of precast concrete segmental beams
642 with hybrid tendons and dry joints. Constr Build Mater 2016;110:1–7.
643 https://doi.org/10.1016/j.conbuildmat.2016.02.003.

644 [24] BonoperaM, ChangK-C, LinT-K, TulliniN. Influence of prestressing on the behavior of
645 uncracked concrete beams with a parabolic bonded tendon. Struct Eng Mech 2021;77:1–17.

646 [25] BonoperaM, ChangKC, ChenCC, SungYC, TulliniN. Experimental study on the fundamental
647 frequency of prestressed concrete bridge beams with parabolic unbonded tendons. J Sound Vib
648 2019;455:150–60. https://doi.org/10.1016/j.jsv.2019.04.038.

649 [26] AASHTO. Standard specifications for highway bridges. 13th ed. The American Association
650 of State Highway and Transportation Officials, Washington DC; 1983.

651 [27] AASHTO. Guide specifications for design and construction of segmental bridges. The
652 American Association of State Highway and Transportation Officials, Washington DC; 1989.

653 [28] TakebayashiT, DeeprasertwongK, LeungYW. A full-scale destructive test of a precast
654 segmental box girder bridge with dry joints and external tendons. Proc Inst Civ Eng - Struct
655 Build 1994;104:297–315. https://doi.org/10.1680/istbu.1994.26780.

656 [29] JensT. Collapse analysis of externally prestressed structures. Diplomica Verlag; 2009.

657 [30] YuenTYP, HalderR, ChenWW, ZhouX, DebT, LiuY, et al. DFEM of a post-tensioned precast
658 concrete segmental bridge with unbonded external tendons subjected to prestress changes.
659 Structures 2020;28:1322–37. https://doi.org/10.1016/j.istruc.2020.09.080.

660 [31] ABAQUS Inc. ABAQUS Analysis User's Manual. 2020.

661 [32] CEN. Eurocode 2: design of concrete structures. Part 1: general rules and rules for buildings
662 (EN 1992–1-1:2004). European Committee for Standardization, Brussels; 2004.

663 [33] YuenTYP, DebT, ZhangH, LiuY. A fracture energy based damage-plasticity interfacial
664 constitutive law for discrete finite element modelling of masonry structures. Comput Struct
665 2019;220:92–113. https://doi.org/10.1016/j.compstruc.2019.05.007.

666 [34] AydanO, MamaghaniIHP, KawamotoT. Application of Discrete Finite Element Method
667 (DFEM) to Rock Engineering Structures 1996.

668 [35] LublinerJ, OliverJ, OllerS, OñateE. A plastic-damage model for concrete. Int J Solids Struct
669 1989;25:299–326. https://doi.org/10.1016/0020-7683(89)90050-4.

670 [36] KrätzigWB, PöllingR. An elasto-plastic damage model for reinforced concrete with minimum
671 number of material parameters. Comput Struct 2004;82:1201–15.
672 https://doi.org/10.1016/j.compstruc.2004.03.002.

673 [37] CEB-FIP. Model Code 2010 - Final version, Vol. 1. vol. 1. fédération internationale du béton,
674 Bulletin 66, Lausanne, Switzerland; 2012. https://doi.org/10.1007/s13398-014-0173-7.2.

675 [38] MaekawaK, OkamuraH, PimanmasA. Non-Linear Mechanics of Reinforced Concrete. 1st ed.
676 CRC Press; 2003.

677 [39] RenW, SneedLH, YangY, HeR. Numerical Simulation of Prestressed Precast Concrete Bridge
678 Deck Panels Using Damage Plasticity Model. Int J Concr Struct Mater 2015;9:45–54.
679 https://doi.org/10.1007/s40069-014-0091-2.

680 [40] ABAQUS Inc. Abaqus User Subroutines Reference Guide. 2020.

681 [41] JiangH, LiY, LiuA, MaZJ, ChenL, ChenY. Shear Behavior of Precast Concrete Segmental
682   Beams with External Tendons. J Bridg Eng 2018;23. https://doi.org/10.1061/(ASCE)BE.1943-
683   5592.0001249.

684 [42] AASHTO. AASHTO LRFD Bridge Design Specifications. 5th ed. American Association of
685   State Highway and Transportation Officials, Washington, DC.; 2010.

686 [43] American Concrete Institute. Building code requirements for structural concrete (ACI 318–19)
687   and Commentary. Farmington Hills, MI: ACI; 2019.

688 [44] Raymond H. Myers, Douglas C. MontgomeryCMA-C. Response Surface Methodology:
689   Process and Product Optimization Using Designed Experiments. 4th ed. WILEY; 2016.

690